11 Surface Physics

T. Greber, R. Holzner, E. Wetli, S. Dangel, T. J. Kreutz, H. Neff,
H. Schmid, P. Schwaller, J. Wider, W. Auwärter, F. Baumberger, S. Berner
M. Hoesch, A. Schneider, W. Deichmann, J. Osterwalder

In the surface physics laboratory we study well-defined surfaces of solid materials as well as adsorbed atomic and molecular monolayers and ultrathin films, prepared under ultrahigh-vacuum (UHV) conditions. In order to obtain detailed information on the geometric arrangement of the atoms within the first few monolayers of the surface we apply predominantly electron-based techniques such as X-ray photoelectron diffraction (XPD), medium-energy electron diffraction (MEED), low-energy electron diffraction (LEED), and most recently also scanning-tunneling and atomic force microscopy (STM/AFM - see below). A time-resolved MEED experiment is being developed with a temporal resolution in the picosecond range. Based on a new experimental geometry for XPD, where photoelectron diffraction effects are measured near a node of the photoexcited electron wave, the concept of photoelectron holography is tested as to whether it could finally fulfill its promises as a direct structural technique on surfaces.

Angle-resolved UV photoelectron spectroscopy (ARUPS) gives access to the electronic band structure of solids and surfaces. Specifically, our experimental setup permits us to directly map sections through the Fermi surfaces of such systems, which represent the electronic degrees of freedom relevant for transport properties, magnetic interactions and phase transitions. We could also extend the measuring range of photoemission above the Fermi level to observe thermally excited electrons within the band structure. An important asset of all these experiments is that the same probe (photoemission) gives structural, electronic and magnetic information, and we can therefore study the interplay between these different degrees of freedom on the same sample.

In a common project with H. Keller we were able to purchase a combined STM/AFM system (Park Scientific) with one measuring head in UHV complementing our electron-scattering based techniques and one head working at ambient pressure serving as a general purpose surface characterization tool for the Physics department and other interested departments. The UHV head is currently being mounted in a dedicated chamber as a stand-alone experiment. After extensive tests this chamber will be connected to our photoelectron spectrometer. The ambient head has found frequent use within our own group and by a group from the Physical Chemistry department (R. Timm, P. Willmott, J. R. Huber).

With this same group we have also had a fruitful collaboration in which they were able to profit from our unique instrumentation for efficiently measuring XPD patterns. It permitted them to perform structural analyses of a large batch of TiN [1] and TiC_xN_{1-x} thin films grown under various conditions. Likewise, we profit from their excellent thin film preparation capabilities using pulsed reactive crossed-beam laser ablation, a technique which was developed in their laboratory, and which is a very clean and versatile version of laser ablation in which the ablated material is brought onto the substrate by a pulsed molecular beam [2].

11.1 The magnetic phase transition of nickel metal

In collaboration with P. Aebi and L. Schlapbach,
Institut de Physique, Université de Fribourg

Nickel metal is the prototypical band ferromagnet. Nevertheless, it has proven difficult to describe the ferromagnetic-to-paramagnetic phase transition, which occurs at $T_c = 631K$, within one consistent theory [3]. A major puzzle remains that neutron scattering experiments find local magnetic moments and spin waves persisting above T_c [4], while photoemission experiments see a Stoner-like collapse of the exchange splitting $\Delta\epsilon_{ex}$ measured between majority ($\uparrow$) and minority ($\downarrow$) bands [5].

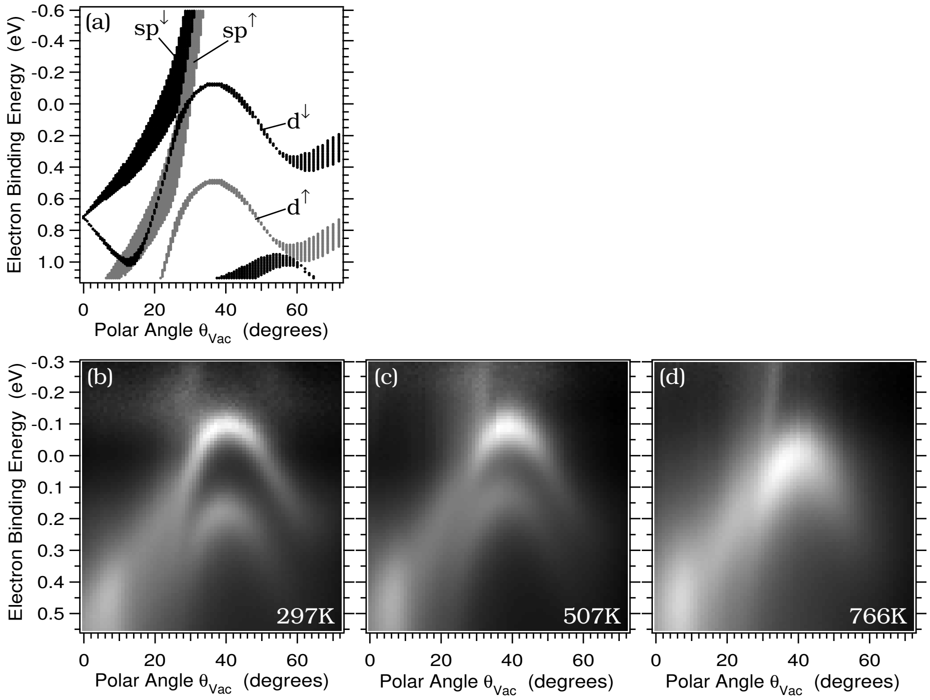

Figure 11.1: (a) - Spin-polarized Korringa-Kohn-Rostoker band structure calculation covering the section in reciprocal space covered by our measurements. Majority spin bands are given in gray, minority bands in black. (b)-(d) : He I excited polar angle scans of photoemission spectra taken from Ni(111), measured at three different temperatures. The data have been divided by the Fermi-Dirac distribution function on the energy scale in order to remove the occupation numbers from the observed bands. The linear gray scale ranges from minimum intensity (white) to maximum intensity (black). The sample temperatures were (b) $T = 0.47T_c$, (c) $0.80T_c$ and (d) $1.21T_c$ from Ref. [6]

.

We have addressed this issue specifically by looking more closely at those regions in wavevector space where the minority d band crosses the Fermi level ϵ_F [6]. Any shift of this band changes the occupation number in this band and is thus directly associated with the average magnetic moment per Ni atom. By means of our clean and intense UV photon source (Gammadata VUV 5000 He discharge lamp with toroidal grating monochromator) we are able to measure band dispersion above ϵ_F in the tail of the Fermi-Dirac distribution function. In Fig. 11.1 b-d the measured bands near the top of the partially occupied d band are shown at different temperatures. Band occupation numbers have been removed by dividing each spectrum, i.e. each vertical line of pixels in these grey-scale plots, by the Fermi-Dirac distribution function. The room temperature data (Fig. 11.1 b) are well described by a band structure calculation for the ground state (Fig. 11.1 a), except for a roughly twofold expansion of the energy scale due to the neglect of on-site Coulomb correlation effects. Nevertheless, all measured bands can be clearly identified, including the fast dispersing sp bands near the apex of the minority d band parabola [7].

The data sets of Fig. 11.1 b-d provide two significant new aspects concerning the magnetic phase transition in Ni:

(1) We have identified a region in $\vec{k}$ space where the minority d band and the two sp bands cross the Fermi level at the same $\vec{k}$ and with nearly the same group velocity. The existence of such a configuration has important implications for the single-particle excitation spectrum. The Stoner gap, normally associated with spin-flip transitions $d^{\uparrow} \rightarrow d^{\downarrow}$, may here be reduced to zero, because transitions of the type $sp^{\downarrow} \rightarrow d^{\downarrow}$ can be strong. In this scenario, the sp band acts as a minority-spin electron reservoir, permitting $d^{\downarrow}$ states to be filled before the $d^{\uparrow}$ band starts being depopulated upon raising the temperature. The related reduction of the average magnetic moment, and thus of $\Delta\epsilon_{ex}$ supplies the positive feedback which drives the phase transition.

(2) A further indication that we have located the magnetically active region which drives the phase transition is, that, above T_c, the top of the coalesced d band is found to lie precisely at the Fermi level. This means that, for this $\vec{k}$ vector the creation of a spin flip costs no energy. Fluctuating local moments and spin waves in the paramagnetic phase are thus fully consistent with our measurements. Indeed, the anomalously large width observed for the normalized spectrum above T_c (Fig. 11.1 d) might be a consequence of these fluctuations.

11.2 Doping-dependent electronic structure of Bi-cuprates

In collaboration with P. Aebi and L. Schlapbach, Institut de Physique, Université de Fribourg, and H. Berger and L. Forro, EPF Lausanne

A current topic in the research field of cuprate high-temperature superconductors is the evolution of the normal state electronic structure with the hole concentration x in the Cu-O layers. The superconducting transition temperature T_c in these materials strongly depends on this concentration. This is illustrated in the inset of Fig. 11.2 where T_c is shown as function of x for $Bi_2Sr_2CaCu_2O_8$ (Bi2212) [8]. Basically three different doping regimes can be distinguished: It exists an optimal doping x_{opt} where the maximum T_c is achieved (labelled *OPT*). T_c decreases if the hole concentration is higher than x_{opt} (overdoped regime, *OD*), as well as for hole concentrations below x_{opt} (underdoped regime, *UD*). Undoped cuprates ($x = 0$) are not superconductors but antiferromagnetic insulators.

The electronic structure of Bi2212 has been investigated by angle-resolved ultraviolet photoelectron spectroscopy (ARUPS) [9]. Our experimental setup [10] allows to measure directly full $k_{||}$-maps of electronic bands of cuprates [11]. We applied this technique to study the doping dependence of the Fermi surface of Bi2212 at 300K. Full Fermi surface maps of overdoped ($T_c = 60K$), optimally doped ($T_c = 84K$) and underdoped Bi2212 ($T_c = 30K$) samples have been measured. The corresponding He I ($21.2eV$ photon energy) excited $k_{||}$-maps are shown in Fig. 11.2a-c. In each pattern the outer circle represents grazing photoelectron emission, the center point normal emission. The photoelectron intensities are represented in a linear grey scale with high intensity given in white. At **k**-locations of Fermi level crossings high intensities occur.

The analysis of these maps yields that the Fermi surface at optimal doping consists

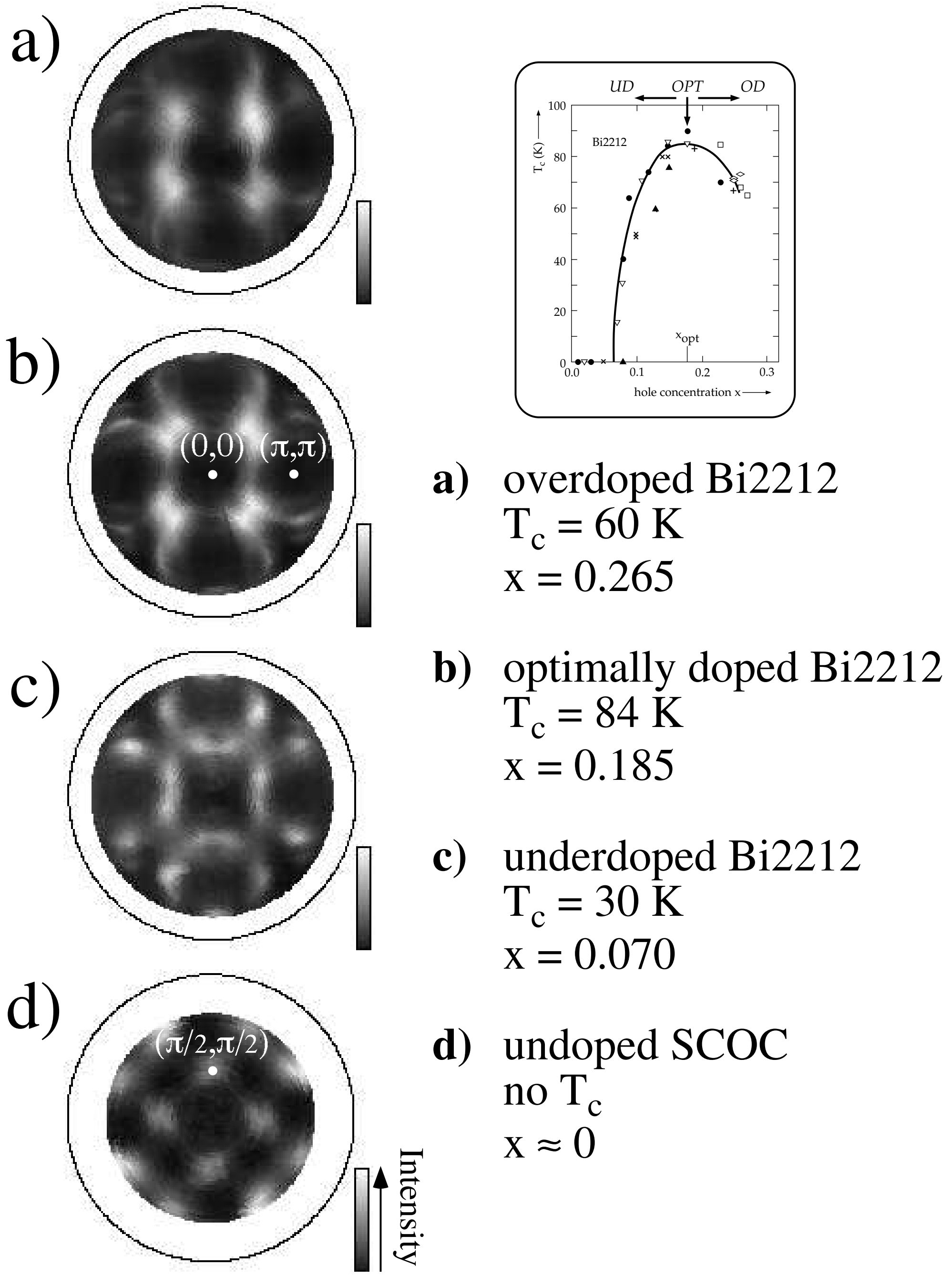

Figure 11.2: He Iα excited photoemission $k_{||}$ maps of cuprates at different doping levels: a) Fermi surface of overdoped Bi2212; b) Fermi surface of optimally doped Bi2212; c) Fermi surface of underdoped Bi2212; d) Valence band maximum map of insulating SCOC. The Fermi surfaces in a-c are raw data, the picture in d has been four-fold averaged. The intensity in all four maps is given in a linear grey scale. The inset shows an experimental T_c vs. hole concentration curve of Bi2212 taken from Ref. [8].

of barrels centered at the (π, π) points, forming a so-called *large Fermi surface* (see Fig. 11.2b). Clearly one can see that the area inside a barrel around (π, π) is shrinking if the hole concentration is lowered. For overdoped and optimally doped Bi2212 we found that this area scales with $(1 + x)$, x beeing the hole concentration [11]. For strongly underdoped Bi2212 with a T_c of $30K$ (Fig. 11.2c) a significant deviation from this $(1 + x)$ behavior is observed. A second strong difference is that the intensity in the $(\frac{\pi}{2}, \frac{\pi}{2})$ region is much higher for underdoped Bi2212 compared to the data at high doping (Fig. 11.2a,b). In underdoped Bi2212 more weight is observed in the same region where the valence band maximum of undoped $Sr_2CuO_2Cl_2$ (SCOC, Fig. 11.2d) is located. This may indicate that the Fermi surface topology is changed at low doping and that small pockets around $(\frac{\pi}{2}, \frac{\pi}{2})$ (so-called *hole pockets*) are formed.

We also studied the influence of high flux UV radiation on the surface region of Bi2212. At room temperature the surface layer of Bi2212 is rather inert to residual gases in ultra-high vacuum. However, strong aging effects under the influence of UV radiation are observed, which limit the measuring time on a pristine surface. A careful analysis of these effects lead us to the conclusion that the UV light is underdoping the surface region of Bi2212 samples [11]. This offers the unique possibility to control the doping level in the surface region and to study the doping dependence of the electronic structure on the same cleaved surface.

11.3 Subsurface oxygen on Rh(111)

In a traditional view of heterogeneous catalysis one pictures all molecular processes to take place on top of a more or less static catalytic surface. The only role of the catalyst is to chemisorb and dissociate the reacting molecules. There have, however, been indications that also the subsurface region of the catalyst may be involved in certain reactions. One system where a subsurface species of oxygen might play an important role as an oxygen reservoir is Rh(111) [12]. We have used XPD in order to observe the occupation of subsurface sites by oxygen atoms directly [13].

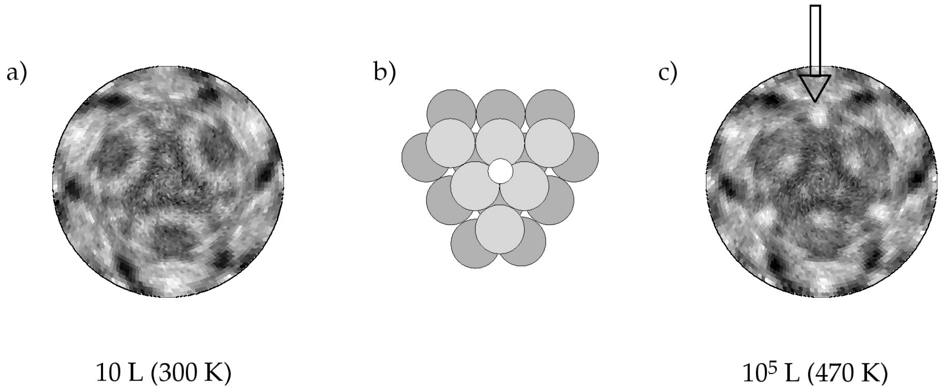

Figure 11.3: a) Mg Kα excited O1s diffractogramm after exposure of 10 L oxygen on Rh(111). The three circular features indicate backscattering from the substrate atoms and allow the identification of the on top adsorbtion site. b) A cluster with two layers of rhodium and one oxygen atom on the surface in the fcc site c) Mg Kα excited O1s diffractogramm after exposure of 10^5 L oxygen. The arrow indicates sharp forward scattering peaks that stem from an ordered subsurface oxygen species.

In Fig. 11.3 a we show the O 1s XPD pattern from a Rh(111) surface which has been exposed to 10 L (1 L (Langmuir) $= 1.33 \cdot 10^{-6}$mbar sec) oxygen at room temperature. Under these conditions it is known that a "clean" adsorbate structure is formed with oxygen atoms occupying so-called fcc sites (Fig. 11.3 b) 1.25Å above the top Rh layer [14], and with no subsurface oxygen present. In a preliminary analysis using single-scattering cluster (SSC) calculations we can well account for all features seen in the XPD pattern, and we can thus fully confirm the structural model obtained by a quantitative LEED study [14].

In Fig. 11.3 c we show the XPD pattern obtained for a surface exposed to 10^5L oxygen at elevated temperature (470 K), conditions that favour the formation of subsurface oxygen. The pattern remains rather similar to the one of Fig. 11.3 a, since the fcc adsorbate site occupation remains predominant. However, significant intensity enhancements appear as indicated by the arrow. Fig. 11.4 a represents a difference plot where the adsorbate site contribution has been removed by subtracting from this data the 10 L data, leaving only subsurface site emission. The resulting pattern is well described by an SSC calculation (Fig. 11.4 b) assuming the occupation of an octahedral site between the first and second Rh layer, which is just underneath the fcc adsorption site. Surprisingly, we find that in the close vicinity of such a subsurface oxygen species the adsorbed oxygen is now occupying hcp adsorption sites (Fig. 11.4 c). This site switch may be highly relevant for the catalytic properties of the oxygen covered Rh(111) surface.

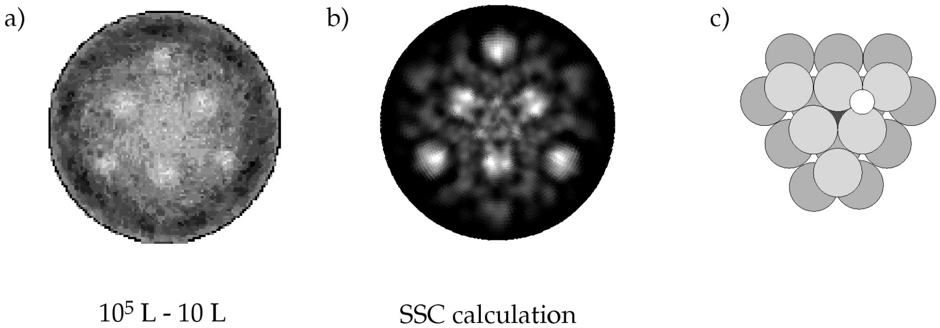

Figure 11.4: a) Difference between Fig. 11.3 c and Fig. 11.3 a. The remaining features are assigned to the subsurface oxygen b) Single scattering cluster calculation (SSC) for the structure as displayed in c). c) Subsurface oxygen in the octahedral site between the first and second rhodium layer. Note the site switch of the on top oxygen (see Fig. 11.3 b).

11.4 Hexagonal boron nitride films on Ni(111)

Monolayers of hexagonal boron nitride have been prepared by the reaction of benzene-like borazine $(BN)_3H_6$ with Ni(111) at 1100 K [15]. A bare nickel surface is a good catalyst for the removal of the hydrogen and therefore the $h-$BN growth rate drops by more than two orders of magnitude after completion of the first layer of boron nitride on Ni(111). The resulting layers are analyzed by means of Si Kα excited N1s and B1s X-ray photoelectron diffraction. In Fig. 11.5 the experimental results are summarized. From the three fold rotational symmetry of the N1s and B1s diffraction pattern it is concluded that the system discriminates fcc from hcp adsorption sites. The higher diffraction anisotropy of the B1s emission pattern compared to that of the N1s pattern indicates that boron emission leads to forward scattering above the surface. From this it is concluded that the $h-$ BN layer is corrugated and that nitrogen terminates the surface. The result is in agreement with an existing LEED analysis on the same system with the structure as shown in Fig. 11.5d) [16]. In the near future these $h-BN$ layers will serve as an insulating spacer layer between nickel and other magnetic materials in order to study the magnetic coupling across insulators.

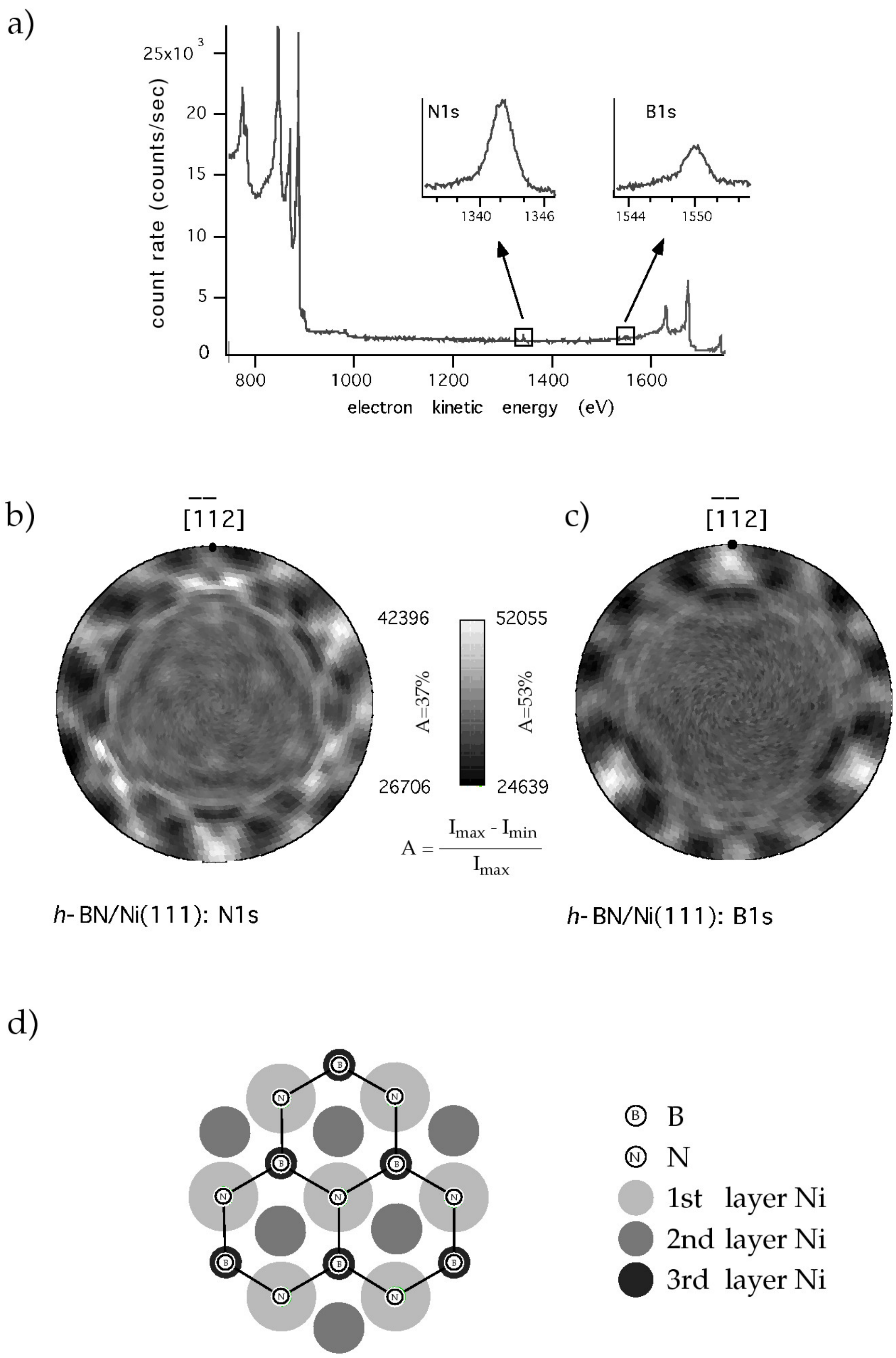

Figure 11.5: Photoelectron diffraction from a monolayer $h-\mathrm{BN}$ on Ni(111). In a) the photoemission spectrum along the surface normal is shown. The insets indicate the B1s and N1s emission respectively. These emission intensities are stereographically projected in b) (N1s) and c) (B1s) on a linear gray scale for 5044 different emission directions into the hemisphere above the surface. In d) the structure as proposed by Gamou et al. [15] is shown.

11.5 Near-node photoelectron holography

Recently it was shown theoretically that Gabor's idea of photoelectron holography for solving new and unknown structures may be realized if forward scattering is suppressed [17, 18]. In an unusual geometry for photoelectron diffraction the photoemission current is measured near a node of the photoelectron source wave. As a consequence forward scattering that obscures holographic reconstruction in the standard geometry is faded out [18].

In May 1997 we started the set up of a new photoelectron diffraction experiment that will meet the requirements for near-node photoelectron holography. To date the chamber with the monochromatized Al Kα X-ray source and the electron analyzer is pumped and set under ultra high vacuum below $5 \cdot 10^{-11}$mbar. In a next step a 2π goniometer that is produced according to an advanced design in our machine shop will be implemented in the experiment (see Fig.11.6). After tests in the standard geometry the analyzer will be moved to the near node geometry.

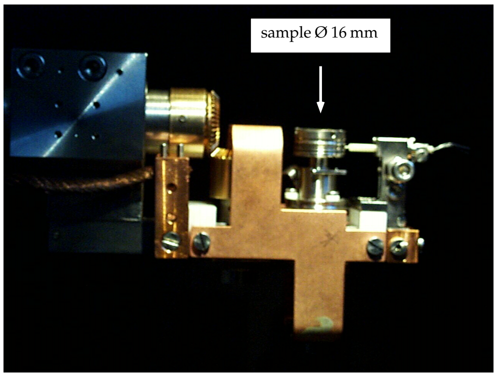

Figure 11.6: Photograph of the new 2π sample goniometer head as produced in our machine shop.

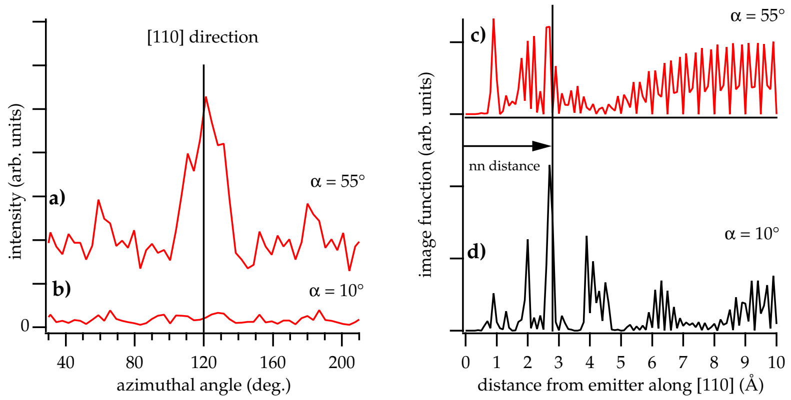

Figure 11.7: Single scattering cluster calculations for Al Kα excited Al2s emission from Al(111). The simulations show an azimuthal scan with a polar angle of 36°. a) Standard geometry with an angle α of 55° between the incoming X-rays and the electron detector b) near-node geometry with an angle α of 10° between the incoming X-rays and the electron detector. It is seen that the forward scattering peak along the [110] direction is suppressed for the near-node geometry. c) and d) show corresponding holographic reconstructions along the [110] direction for c) the standard and d) the near-node geometry. It shows that for the near node geometry the nearfield contribution of forward scattering is suppressed and that the most prominent peak can be interpreted as an image of an atom close to the nearest neigbour (nn) distance.

With further single scattering cluster calculations candidate systems for the first experimental demonstration of near-node photoelectron holography have been evaluated. Since the photoemission intensity drops substantially in measuring the photoemission current near a node of the source wave it is appropriate to start with the analysis of a bulk substrate where several atomic layers contribute to the emission instead of a single layer as proposed in [17]. In Fig.11.7 it is shown that Al is a valuable candidate for the demonstration of holographic reconstruction from near node photoelectron emission data.

11.6 Time-resolved medium-energy electron diffraction

In collaboration with M. Aeschlimann, Institut für Technische Chemie, ETHZ

We have been working on the design of an experimental method for obtaining structural information on solid surfaces on a very short time scale. We are following a scheme where we generate a pulsed electron beam of typically 2 keV energy and measure the angular distribution of the backscattered electrons on a channelplate detector (medium-energy electron diffraction (MEED), also named secondary electron imaging (SEI) - this technique has been largely developed by M. Erbudak at ETHZ [19]). Figure 11.8 shows the realised experimental setup with the home built electron gun (following the design of Ref. [20]), the channelplate electron detector, and the sample holder which can be cooled and rotated. For sample cleaning we have the possibility of ion bombardment. With the same electron detector we can run Auger electron spectroscopy for chemical surface analysis.

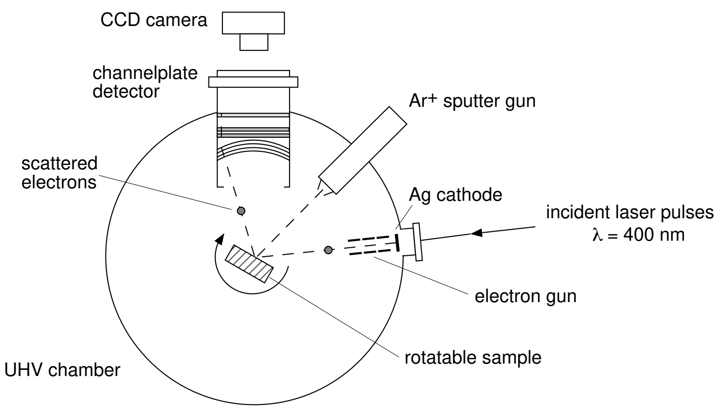

Figure 11.8: Experimental setup of the MEED chamber. Incoming electrons hit the surface at an incidence angle of 85° with respect to the center of the electron detector.

The electron pulses are produced by shining femtosecond laser pulses (duration about 100 fs) on a photocathode. Considering the electron optical properties of our electron gun we expect electron pulses of a few picoseconds in width. The number of electrons in a single pulse is naturally not sufficient to create a measurable diffraction pattern on the screen and we thus have to operate the experiment in a pump-probe mode where we periodically prepare the surface in a defined way at a certain time t_0 and have the electron pulse impinge on the surface with a defined delay dt. In order to achieve picosecond resolution in the delay, the preparation step must necessarily be triggered by a laser pulse which is temporally correlated with the probe electron pulse.

We have a Ti:saphire laser system (Figure 11.9) available in our laboratory producing femtosecond pulses of nanojoule energies. This laser works at a wavelength of 800 nm. For the production of the electron pulses at the photocathode we have to double the optical frequency. For that purpose we use a nonlinear single crystal (BBO). To enhance the photoelectron cur-

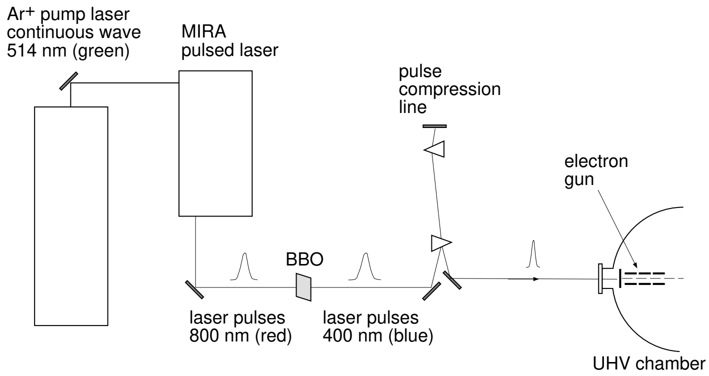

Figure 11.9: Setup for the production of pulsed electrons by a fs-laser system

rent on the cathode we have built a pulse compression line for higher photoemission efficiency. We can use a fs-laser Coherent/Mira borrowed from the Physical Chemistry department for the laser puls production which is pumped by our Ar ion laser. In the next future we will change to a Verdi pump laser by Coherent and move the experiment into a new laboratory. At the moment our MEED scattering chamber is working nicely and first experiments with our pulsed electron gun have proved the feasibility of this experiment.

In our setup the electrons can hit the sample surface at grazing incidence for enhancing the surface sensitivity of the MEED experiment. To explore this sensitivity we use a well known Si(001) surface as a test sample. Si(001) undergoes a dynamical structural change in the topmost atomic layer at 250 K. At room temperature the clean Si(001) surface exists in a reconstructed (2x1) dimers configuration and changes to a c(4x2) structure below 250 K. This change can easily be observed by LEED as a change in the surface periodicity. The MEED technique may potentially deliver information on the atomic arrangement within the surface unit cell in real space if the surface sensitivity can be sufficiently enhanced. Figure 11.10 shows recorded MEED patterns of the Si(001) surface at 200 K, taken at three different sample rotation angles. The visible intensity features show the angle dependent scattering of the incoming electrons. The rotation angles of the sample and of the diffraction features are the same - this behaviour is typical for processes in real space.

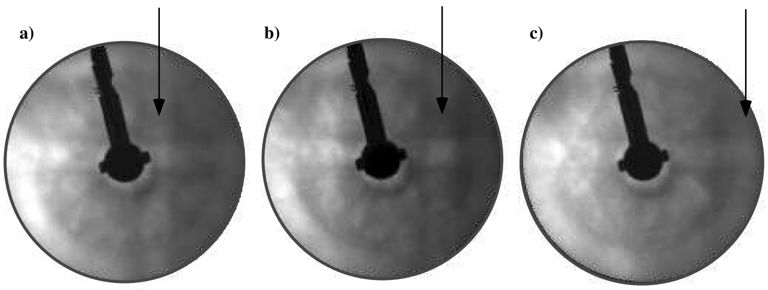

Figure 11.10: MEED patterns of Si(001) at different sample rotational angles: a) 10°, b) 20°, c) 30°. The arrows indicate intensity features, rotating with the sample. The shadow of the second electron gun is visible in the center of the detector.

A particular feature, which is associated with scattering along the [001] direction, is indicated by the arrows. Most of the observed features are rather bulk sensitive. Our current analysis tries to unravel subtle changes that occur at the phase transition temperature, and that would indicate top layer sensitivity.

11.7 Towards a 2d-vapor of sodium atoms

When a surface is exposed to sodium vapor in a UHV chamber at room temperature, sodium atoms may be deposited on the surface either as single atoms, clusters or as a thin 2-dimensional film. Our aim is to demonstrate under these conditions laser-atom-interaction effects previously observed in a normal, three dimensional vapor [21]. One of these effects, called beamswitching [22], where one circularly polarized laser beam switches off another laser beam of opposite circular polarization may be of interest with regard to nanoscale all optical logical gates. Two dimensional in this context means, that the sodium atoms can freely move in two dimensions while their propagation in the third dimension is restricted to less than about 0.5 microns which is about the wavelength of the atomic D1 transition of sodium.

On our way to this goal we have developed a sandwich type sodium vapor cell which can be "loaded" by an electrical current operated sodium dispenser in UHV (fig.11.11).

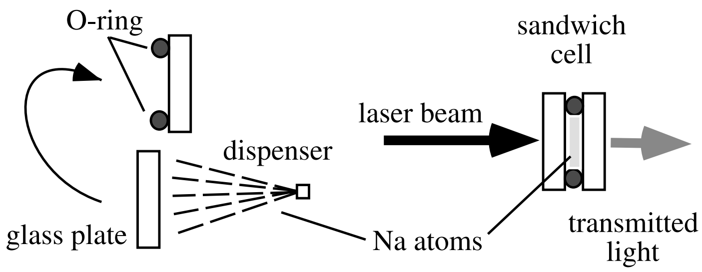

Figure 11.11: Loading of a sandwich cell by a sodium dispenser in UHV

After one glass plate has been sufficiently coated it can be rotated and closes the cell by pressing against the Viton O-ring mounted on the other glass plate. A suitable laser beam, which may or may not be resonant to the atomic D1 transition of sodium, is then directed through the sandwich cell. Due to absorption in the coating the cell heats up and sodium atoms evaporate inside the cell.

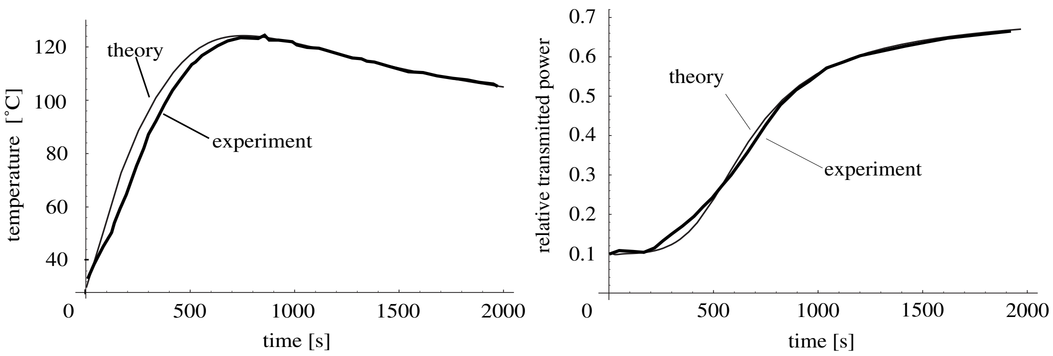

Figure 11.12: Comparison between the measured and the calculated cell temperature and light transmission of the sandwich cell

The cell temperature as well as the transmitted light from the laser beam are measured and compared (fig.11.12) to the values from an according model for the energy flows between the glass plates, the conversion between the input light, sticking coefficients of sodium on glass as well as energy losses due to black body radiation, heat conduction to the UHV chamber and the leakage rate of the cell. In a next step the spacing between the plates is reduced to about 0.5 microns in order to obtain the wanted 2d sodium vapor.

References

[1] R. Timm, P. R. Willmott, J. R. Huber, Appl. Phys. Lett. **71** (1997) 1966.

[2] P. R. Willmott, R. Timm, P. Felder, J. R. Huber, J. Appl. Phys. **76** (1994) 2657.

[3] H. Capellmann, *Metallic Magnetism* (Springer, Berlin, 1987).

[4] G. Shirane, O. Steinsvoll, Y. J. Uemura, J. Wicksted, J. Appl. Phys. **55**, 1887 (1984).

[5] M. Donath, Surf. Sci. Rep. **20**, 251 (1994).

[6] T. Greber, T. J. Kreutz, J. Osterwalder, Phys. Rev. Lett. **79**, 4465 (1997).

[7] T. J. Kreutz, PhD thesis, University of Zürich (1997).

[8] W. A. Groen, D. M. de Leeuw, and L. F. Feiner, Physica C, **165** (1990) 55.

[9] Z.-X. Shen, W. E. Spicer, D. M. King, D. S. Dessau, and B. O. Wells, Science **267**, (1995) 343.

[10] T. Greber, O. Raetzo, T. J. Kreutz, P. Schwaller, W. Deichmann, E. Wetli, and J. Osterwalder, Rev. Sci. Instrum. **68**, (1997) 4549.

[11] P. Schwaller, PhD thesis, University of Zürich (1997).

[12] K. A. Peterlinz, S. J. Sibener, J. Phys. Chem. **99**, 2817 (1997).

[13] J. Wider, T. Greber, E. Wetli, T. J. Kreutz, P. Schwaller, J. Osterwalder, submitted to Surf. Sci.

[14] S. Schwegmann, H. Over, V. De Renzi, G. Ertl, Surf. Sci. **375**, 91 (1997).

[15] Y. Gamou, M. Terai, A. Nagashima, C. Oshima, Sci. Rep. RITU **A44**, 221 (1997).

[16] A. Nagashima, N. Tejima, Y. Gamou, T. Kawai, C. Oshima, Phys. Rev. B **51**,4606 (1995).

[17] T. Greber, J. Osterwalder, Chem. Phys. Lett. **256**,653 (1995).

[18] T. Greber, J. Osterwalder, Prog. Surf. Sci. **53**,163 (1997).

[19] M. Erbudak, M. Hochstrasser, E. Wetli, and M. Zurchkirch, Surf. Rev. Lett. **4** (1997) 179.

[20] M. Aeschlimann, E. Hull, J. Cao, C.A. Schmutternmaer, L.G. Jahn, Y. Gao, H.E. Elsayed-Ali, D.A. Mantell, and M.R. Scheinfein, Rev. Sci. Instrum. **66** (2) (1995) 1000.

[21] R. Holzner, J. Simonet, L. Flepp, B. Röhricht, P. Eschle, S. Dangel, U. Rusch, H. Schmid, and E. Brun. Using nuclear spins, radio waves, sodium atoms, and laser light to investigate spatiotemporal nonlinear systems. *Optical Engineering*, 34:2315–2323, 1995.

[22] S. Dangel, P. Eschle, B. Röhricht, U. Rusch, H. Schmid, and R. Holzner. Dynamics of laser beam switching in sodium vapor. *J. Opt. Soc. Am. B*, 12(4):681–686, 1995.